

# Regulating Li Uniform Deposition by Lithiophilic Interlayer as Li-ion Redistributor for Highly Stable Lithium Metal Batteries

Xiaojuan Zhang<sup>1, 2, 3</sup>, Yuanfu Chen<sup>1, 4\*</sup>, Fei Ma<sup>1</sup>, Xin Chen<sup>1</sup>, Bin Wang<sup>1</sup>, Qi Wu<sup>4</sup>, Ziheng Zhang<sup>1</sup>, Dawei Liu<sup>1</sup>, Wanli Zhang<sup>1</sup>, Jiarui He<sup>1\*</sup>, Zheng-Long Xu<sup>2, 5, 6\*</sup>

<sup>1</sup> School of Electronic Science and Engineering, and State Key Laboratory of Electronic Thin Films and Integrated Devices, University of Electronic Science and Technology of China, Chengdu 610054, PR China

<sup>2</sup> Department of Industrial and Systems Engineering, The Hong Kong Polytechnic University, Hong Kong SAR, PR China

<sup>3</sup> College of Optoelectronic Engineering, Chengdu University of Information Technology, Chengdu 610054, PR China

<sup>4</sup> College of Science and Institute of Oxygen, Tibet University, Lhasa, 850000, PR China

<sup>5</sup> State Key Laboratory of Ultraprecision Machining Technology, The Hong Kong Polytechnic University, Hong Kong SAR, PR China.

<sup>6</sup> Research Institute of Smart Energy, The Hong Kong Polytechnic University, Hong Kong SAR, PR China.

\*Corresponding authors.

Emails addresses: [yfchen@uestc.edu.cn](mailto:yfchen@uestc.edu.cn) (Y.F. Chen)

E-mail: [hejiarui123@sina.com](mailto:hejiarui123@sina.com) (J. R. He)

E-mail: [zhenglong.xu@polyu.edu.hk](mailto:zhenglong.xu@polyu.edu.hk) (Z. L. Xu)

**Abstract:**

Although Lithium (Li) metal anode possesses a high theoretical capacity and low redox potential, the poor cycling stability and safety concerns caused by Li dendrites seriously hinder the implementation of Li metal-based batteries. Herein, for the first time, we present a novel interlayer of lithiophilic  $W_2N_3$  embedded N-doped graphene (WNG) as Li-ion redistributor to effectively adjust and redistribute the interfacial ionic flux. Due to its unique porous nanoarchitecture, WNG nanosheets can guarantee robust mechanical strength, excellent thermal stability and abundant Li deposition sites, meanwhile  $W_2N_3$  nanoparticles with the abundant polar bonds can offer a strong interaction between Li atom and  $W_2N_3$  to uniformly regulate the interfacial Li-ion flux thus effectively inhibiting the growth of Li dendrites. DFT calculations further confirms a strong interaction between Li atom and WNG, and the Li ion concentration using WNG/PP is 11.3 times lower than that using bare PP separator. As a result, the lithium metal batteries with WNG interlayer demonstrate dendrite-free and ultra-stable features: the Li//Li symmetric cells show ultralow overpotential (49.6 mV) at ultra-long-term cycling of 2000 h even at  $5 \text{ mA cm}^{-2}$  with  $1 \text{ mAh cm}^{-2}$ ; the Li//LiFePO<sub>4</sub> full cells exhibit exceptionally ultra-low capacity decay rate of 0.06%/cycle after 300 cycles.

**Keywords:** Lithiophilic  $W_2N_3$ ; N-doped graphene; Li-ion redistribution; DFT calculations; Li metal batteries

## 1. Introduction

Lithium (Li) metal anode has drawn significant attention for use in high-energy rechargeable batteries due to its lightweight density ( $0.53 \text{ g cm}^{-3}$ ), exceptionally low reduction potential ( $-3.04 \text{ V}$  vs. standard hydrogen electrode) and high theoretical capacity ( $\sim 3860 \text{ mAh g}^{-1}$ ). These properties are superior to graphite anodes ( $372 \text{ mAh g}^{-1}$ ) used in commercially available Li-ion batteries [1-4]. Moreover, the high-capacity Li metal anode allows combination with non-lithiated cathodes, such as sulfur and oxygen, to accomplish high energy Li-S, Li-O<sub>2</sub> battery technologies [5-7]. Therefore, lithium metal batteries (LMBs) are expected to satisfy the future demands on diverse high energy storage systems. However, the commercialization of LMBs is strictly constrained by the inevitable growth of Li dendrites, limited cycle life and continuous side reactions between chemo-mechanical unstable Li deposition (or Li dendrite) and electrolyte during the battery cycling [8-10].

To mitigate the above challenges, several strategies have been developed over the past decade, such as the optimization of electrolyte compositions [11-15], engineering artificial solid electrolyte interphases (SEI) [16, 17], modification of the electrolyte/electrode interface [18] and construction of innovative Li metal host [19-21]. Some of these approaches are useful to regulate Li ion deposition by governing the Li ion flux and diffusion kinetics, with others effective in tuning the electrode/electrolyte interfacial chemistry and Li metal deposition sites, which has resulted in appreciable improvement in LMB performance. However, less attention has been paid to engineering the separator, which is another critical component determining the Li-ion migration dynamics and influencing the Li ions mass transport/diffusion in LMBs [22]. In general, Li ion transport between electrodes is only accomplished through the electrolyte adsorbed in the separator [23]. Due to the ion-insulating nature of the commercial polypropylene (PP) separator, the Li ion

distribution passing through the separators is uneven with higher concentration around the pores than that behind the PP separator, which intrinsically cause uneven deposition of Li <sup>[22]</sup>. Based on a review of previous studies, there is a potential solution to overcome the issue of Li dendrite growth by regulating the Li-ion diffusion/transport through the functionalized separator, consequently prolonging the life span of battery. To regulate the Li ion migration through separators, polymer <sup>[24, 25]</sup>, boron-nitride <sup>[26]</sup>, organic molecules <sup>[27]</sup>, and ceramics <sup>[28]</sup> have been coated on separators. However, these material coatings may cause additional interfacial resistance problem and the fundamental problem of uneven Li deposition is still insoluble, that may finally aid the non-uniform growth of Li dendrites <sup>[26, 29]</sup>. Recently, it was found that the use of lithiophilic polyacrylamide-grafted graphene oxide molecular brushes coated on PP separators with abundant polar bonds/functional groups can make Li-ion flux uniform on the electrode surfaces and thus promote uniform Li deposition <sup>[30]</sup>. Unfortunately, the mechanical strength of lithiophilic separators are too poor to withstand the great pressure from the huge volume change of Li metal anode <sup>[31]</sup>. Therefore, it is a major challenge to develop advanced separators that simultaneously possess robust mechanical strength, high ionic conductivity, and valuable lithiophilic features to boost the electrochemical performance of Li metal anodes under high current densities.

Thanks to the appealing features of excellent thermal and chemical stability, strong mechanical strength (>10 GPa), outstanding catalytic activity and high conductivity <sup>[32, 33]</sup>, transition metal nitrides (TMNs) have been extensively applied in energy storage systems and electronic devices. Among the numerous TMN compounds, tungsten nitrides (WN<sub>x</sub>) are fundamentally appealing to modified separator applications, due to its ultrahigh Young's modulus of 430 GPa, excellent thermal and chemical stability, remarkable conductivity ( $6.97 \times 10^3 \text{ S m}^{-1}$ )

[34]. These features enable strong mechanical strength and fast charge transfer kinetics for the hypothetical  $WN_x$ -modified PP separators. Unfortunately, compared to the preparation of transition metal oxides, it is much more difficult to obtain desirable TMNs due to the requirements of the stringent anaerobic, anhydrous and high temperatures conditions. As a result, to the best of our knowledge, no  $WN_x$ -modified separator has yet been reported to regulate Li deposition for high-performance LMBs.

In this work, for the first time, by optimizing synthesis, we prepared a tungsten nitrides ( $W_2N_3$ ) embedded nitrogen-doped graphene (WNG) composites by a facile hydrothermal method and followed ammonization methods to modify PP separators for dendrite-free LMBs. Based on comprehensive density functional theory (DFT) calculations, we find that WNG presents the strongest affiliation with Li ions among  $WN$ ,  $W_2N$ ,  $W_2N_3$  and WNG. Together with the features of superior electrolyte wettability, high Li-ion conductivity and transference number, the WNG functionalized PP (WNG/PP) separator is capable to trap and redistribute the Li ion flux passing through the separators. The amended Li ion distribution is also elucidated by finite element calculation, which shows that the standard deviation of the Li-ion concentration after WNG/PP separator is 11.3 times smaller than that for pristine PP separator. The mechanically strong and porous WNG/PP further uniforms the Li deposition by mechanical compression and rapid electrolyte penetration. As a result, homogeneous and fast Li ion flux is achieved with the multi-functional WNG modified PP separators, leading to dendrite-free Li metal deposition with ultralong cycle life at high current densities. In conjunction with  $LiFePO_4$  cathodes, the  $Li//LiFePO_4$  full cells using WNG/PP separators delivers outstanding reversibility over 300 cycles at 1C with high coulombic efficiencies. This work provides new insight and a general strategy to

regulate Li ion deposition by use of a functionalized separator to achieve protection of Li metal anodes in rechargeable batteries.

## 2. Results and Discussion

### 2.1 Selection of optimal tungsten nitrides based on mechanistic insights

To select proper  $WN_x$  for effective Li ion flux regulation, the adsorption energies of various  $WN_x$  (i.e., WN,  $W_2N$  and  $W_2N_3$ ) towards Li atom have been thoroughly examined by DFT calculations. The thermodynamically favorable WN (111) and  $W_2N$  (200) surfaces were developed to investigate the Li atom adsorption (**Figure S1**). For the WN surface, there are two possible Li adsorption sites, namely, the terminal N atom with an adsorption energy of -3.20 eV, and the terminal W atom with -2.67 eV (**Figure 1a-b, Figure S2a-b**). For the  $W_2N$  (200) surface, the N-top site and W-top site present comparable adsorption energies of -2.54 eV and 2.58 eV, respectively (**Figure 1d-e, Figure S2c-d**), suggesting similar Li adsorption stability. Due to the unique structure of  $W_2N_3$  (002) surface, only one terminal atom of N-top site is available for Li adsorption, as presented in **Figure S3a-b**. The  $W_2N_3$  exhibits greater adsorption energy of -4.40 eV on the N-top site (**Figure 1g, Figure S3c**), suggesting higher affinity for Li on  $W_2N_3$  than that WN and  $W_2N$ . Meanwhile, the charge density differences in **Figure 1c, f and i** demonstrate a stronger interfacial interaction of Li atom with the  $W_2N_3$  surface in comparison to the WN and  $W_2N$  surfaces. Thus, it can be inferred that Li atom will have stronger interactions with the  $W_2N_3$  (002). It should be able to adjust and redistribute the concentration gradient of Li-ions.  $W_2N_3$  was therefore selected as the substrate material for the following target functional materials.

By integrate material structure and property,  $W_2N_3$  embedded nitrogen-doped graphene (WNG) was prepared and applied to Li metal batteries (LMBs). To check whether the compositing structure would impact the superior Li adsorption capability on  $W_3N_2$ , we also examined the WNG

materials by DFT calculations. **Figure S4, 1h** show the DFT calculated NG sheet configuration, which presents an adsorption energy of -2.88 eV. The predicted configuration of Li adsorption on WNG is exhibited in **Figure S5, S6**, where Li atom has two adsorption positions (**Figure 1j-k** and **S6**). When the Li atom is centered on the top of the NG sheet in WNG, it is evident that the adsorption energy of -3.88 eV is primarily attributed to NG sheet (**Figure 1j, S6a**). This adsorption energy is considerably higher than that of Li adsorption on a pure NG sheet, suggesting more favorable for deposition on WNG. Conversely, when Li atom is centered between  $W_2N_3$  and the NG sheet, the adsorption energy is -4.73 eV (**Figure 1k, S6b**), which is higher than that of Li centered on the top of NG sheet in WNG composite (**Figure 1m**), indicating that Li situated between  $W_2N_3$  and NG sheet is more stable and more favorable for deposition. Based on the DFT calculations, it can be inferred that the most stable and favorable position for the Li deposition is likely between  $W_2N_3$  and NG sheet. The charge density differences presented in **Figure 1i** and **1l** also demonstrate stronger interfacial interactions of Li towards WNG in comparison to  $W_2N_3$ . The adsorption energies for different predicted configurations are presented in **Figure 1m**, which clearly illustrates that WNG exhibits the strongest adsorption energies to Li atom.

Based on the above theoretical calculations, the schematic illustration of the WNG interlayer optimized for adjusting and redistributing Li ion flux and concentration gradients is presented in **Figure S7**. **Figure S7a** was the typical process of Li dendrite growth and nucleation of the cell with pristine PP separator. Large quantities of Li dendrites can be formed and growing due to the difference in potentials between the tip and base of the dendrite with the concentrating electric field effect<sup>[35]</sup>. After long-term cycles, the growing Li dendrites can puncture the PP separator resulting in the internal shorting of the cell or thermal runaway. In contrast, the WNG coating layer can play

an important role to adjust and redistribute Li-ion distribution by taking advantage of the abundant ion conduction channels and stronger interaction with Li (**Figure S7b**). Different from the case for bare PP separator, the Li deposition on surfaces of the Li anode was dense and smooth bowl-shaped. It is likely due to the WNG coating layer dispersing the Li ions in the electrolytes creating a uniform concentration and flux near the surface of anode. This strategy can provide pathway to enable the uniform distribution of Li ions and convert Li dendrites into dense and smooth deposition Li. In addition, the WNG/PP separator has a high mechanical modulus, preventing Li dendrites from penetrating the separator from another aspect. These results verify that the incorporation of  $W_2N_3$  into NG sheets is expected to achieve enhanced interactions with Li atom and adjust the concentration gradient and flux of Li-ion, resulting in a stabilized Li metal anode.

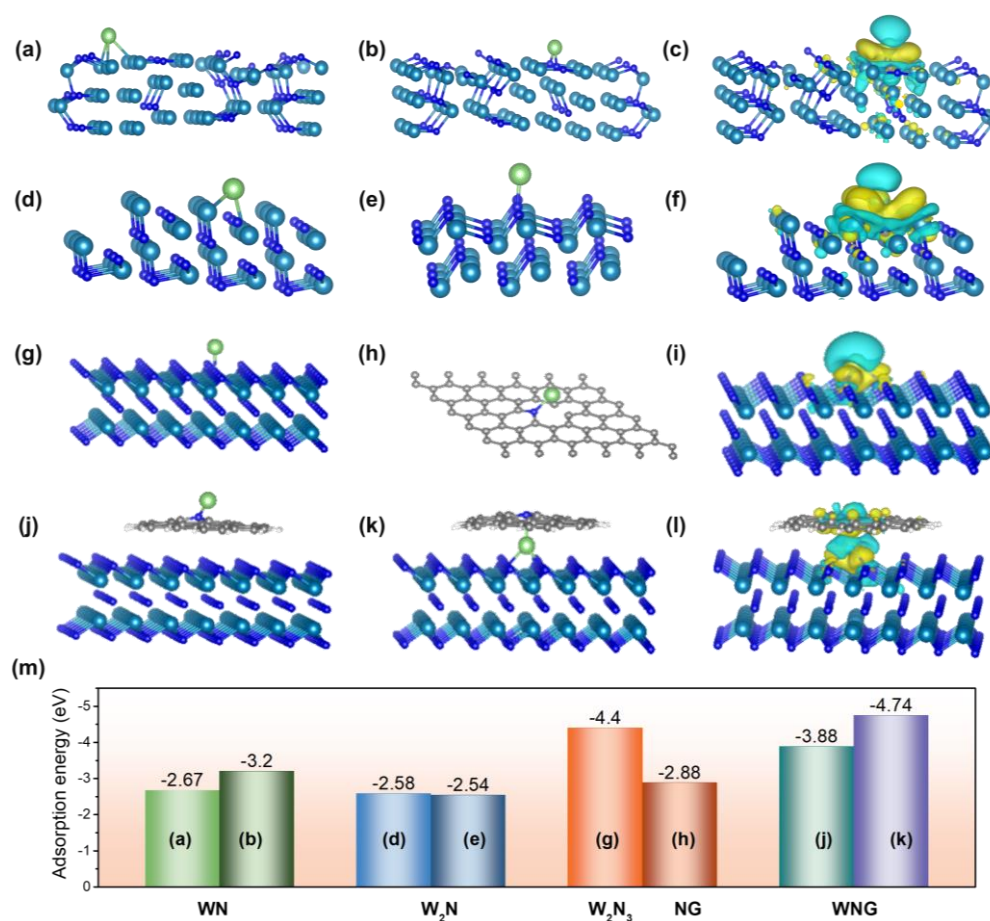


**Figure 1.** Front-view of predicted configurations and absorption energy comparison. (a, b) Li on

WN, (d, e) W<sub>2</sub>N, (g) W<sub>2</sub>N<sub>3</sub> and (h) NG. (j) Li on the top of NG sheet in WNG and (k) Li between W<sub>2</sub>N<sub>3</sub> and NG. Charge density differences of Li on the surfaces of (c) WN, (f) W<sub>2</sub>N, (i) W<sub>2</sub>N<sub>3</sub> and (l) WNG. The yellow and cyan spheres represent electron accumulation and depletion, respectively. The iso-surface level is 0.001 e Å<sup>-3</sup>. (m) the adsorption energy comparison for different predicted configurations.

## 2.2 Synthesis and characterization of WNG

To confirm above theoretical hypothesis, we prepared and characterized the WNG composite as following. Given the dramatically high formation energy of the W-N bond, synthesis of W<sub>2</sub>N<sub>3</sub> usually requires tightly controlled conditions, *i.e.*, pressures of above 5 GPa and temperatures of over 1480 K [36, 37]. In this work, we designed a simpler and effective method to synthesize W<sub>2</sub>N<sub>3</sub>, for the first time. The WNG containing the ultrathin W<sub>2</sub>N<sub>3</sub> nanoflakes embedded into nitrogen-doped graphene was one-pot fabricated by mixing a complexing agent and salt via hydrothermal method and followed by ammonification at atmospheric pressure (**Figure 2a**, see details in Experimental Section in the Supporting Information). The first stage involved the hydrothermal assembly of WO<sub>x</sub>·xH<sub>2</sub>O on graphene oxide (GO) sheets. In the following ammonification process, the interwoven WO<sub>x</sub>·xH<sub>2</sub>O@GO was transformed to ultrathin W<sub>2</sub>N<sub>3</sub> nanoflakes inner-embedded N-doped graphene by displacement and heteroatom doping reaction, respectively. During the ammonization reaction, the nanopores were also generated by the removal of water molecules and the strain release as well as the exchange between atoms. The porosity was determined by Brunauer-Emmett-Teller (BET) surface area analysis. The WNG delivers a surface area of 30.34 m<sup>2</sup> g<sup>-1</sup> with an average pore size of 19.2 nm, which are comparable to 12.49 m<sup>2</sup> g<sup>-1</sup> and 17.0 nm for pure W<sub>2</sub>N<sub>3</sub> (**Figure S8**). The abundant nanopores and moderate surface area are favorable to electrolyte adsorption and wettability as well as decreasing local current density [38], to be discussed later, which are beneficial to fast Li ion diffusion and inhibiting Li dendrite formation in working LMBs.

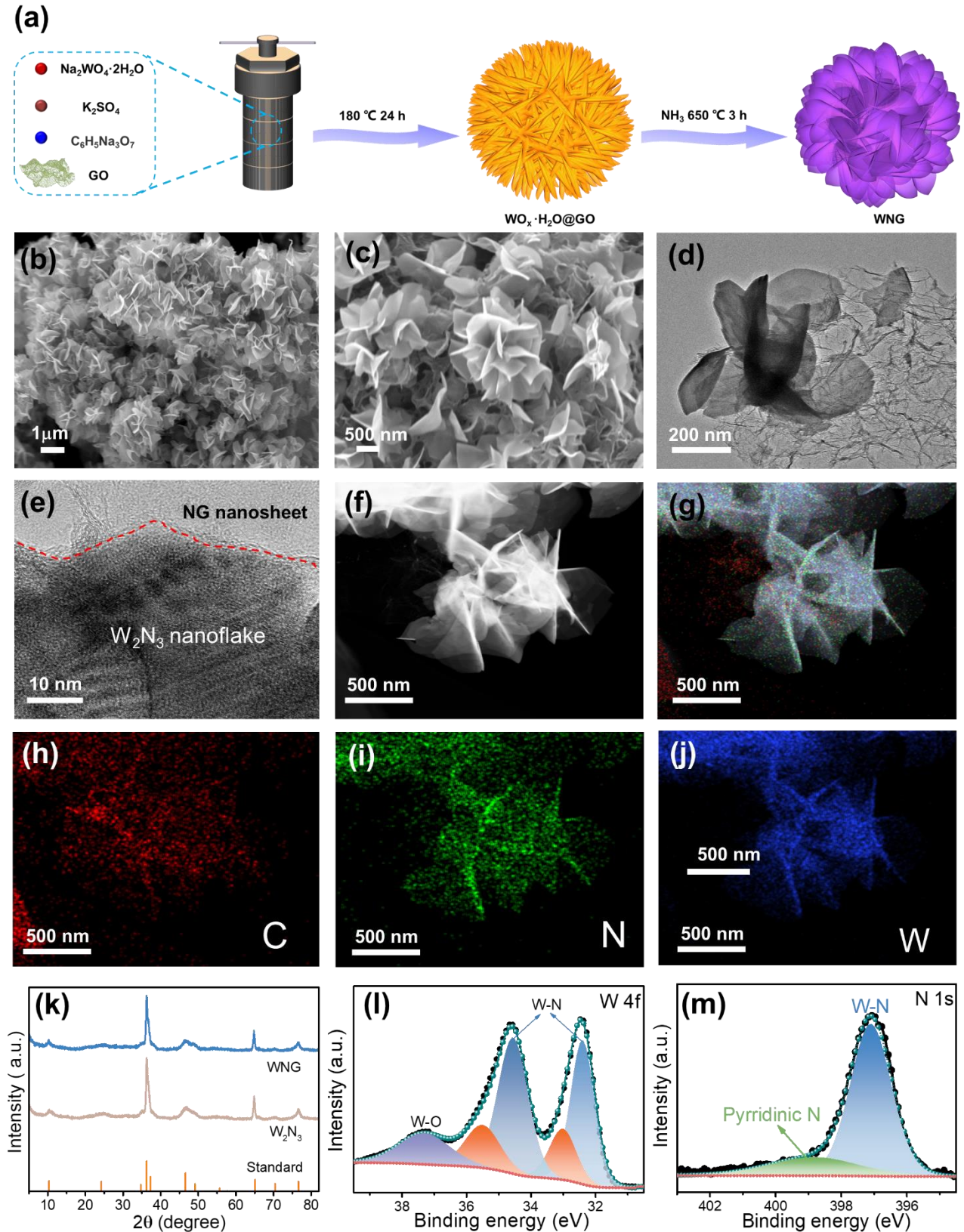


**Figure 2.** Synthesis and characterizations of the WNG functional materials. (a) Schematic of the synthesis and application of a WNG. (b, c) SEM image of WNG. (d) TEM and (e) HR-TEM of WNG. (f-j) HAADF-EDX elemental mappings of WNG showing the uniform spatial distribution of (h) C, (i) N and (j) W. (k) XRD patterns and XPS spectrum of (l) W 4f, (m) N 1s of WNG.

The morphology and structures of the WNG materials were examined by field-emission scanning electron microscopic (FE-SEM, **Figure 2b-c**) and transmission electron microscopy (TEM, **Figure 2d-j**). WNG exhibits a nanoflower-shaped structure composed of ultrathin  $W_2N_3$  embedded in NG nanosheets (**Figure 2b-d**). The HRTEM image (**Figure 2e**) clearly illustrates adhesion of  $W_2N_3$  particles on NG nanosheets, corroborating the structure. HAADF-EDX elemental mapping of WNG (**Figure 2f-j**) clarifies the uniform spatial distribution of C (**Figure 2h**), N (**Figure 2i**) and W (**Figure 2j**). To determine a clear morphology, the SEM images of the precursors and products after ammonization with different complexing agents have been provided (**Figures S9-10**). The  $W_2N_3$  was also prepared as control sample, which displays a nanoflower structure with thick sheets (**Figure S11**). The chemical structures of WNG were determined by X-ray diffraction (XRD) and X-ray photoelectron spectroscopy (XPS) characterizations. **Figure 2k** shows that the XRD patterns of  $W_2N_3$  and WNG are well described by the standard pattern <sup>[39]</sup>, indicating the pure crystallinity of  $W_2N_3$  prepared in this work. It is noted that the diffraction peak of graphene in the WNG is marginally detected, possibly due to the low proportion of graphene in the composite. The general XPS spectrum in **Figure S12a** clearly illustrates the presence of W, N, and C elements in WNG sample, consistent with the TEM-EDS mapping result. The deconvoluted XPS spectra of the W 4f (**Figure 2i**) included two main peaks at  $\approx 34.6$  and  $\approx 32.5$  eV, corresponding to the W 4f<sub>5/2</sub> and W 4f<sub>7/2</sub> characteristic peaks of  $W_2N_3$ , respectively <sup>[40]</sup>. A marginal W peak at  $\approx 37.3$  eV was attributed to inevitable surface oxidation during sample preparation for XPS analysis <sup>[41]</sup>. For the N 1s spectra (**Figure 2m**), two peaks at about 397.0 eV and 398.8 eV assigned to W-N bond <sup>[42]</sup> and pyridinic N, respectively, are deconvoluted. The C 1s spectra (**Figure S12b**) can be deconvoluted into five sub-peaks at 284.6 eV, 285.5 eV, 286.5 eV, and 289.1 eV,

respectively. The binding energy (BE) of 284.6 eV represent the graphitic carbon with C–C, C=C and C–H bonds [43, 44]. The BE of 285.5 eV is ascribed to the C–N bonds in carbon. This suggests that the NH<sub>3</sub> annealing not only react with tungsten compounds to form N–W bond, but also introduce N doping in graphene host. The peaks at 286.8 eV and 288.6 eV can be indexed to the C–O and C=O bonds, respectively. Above XPS characterizations demonstrate the successful preparation of W<sub>2</sub>N<sub>3</sub> nanoflowers embedded in NG sheets.

### 2.3 Evaluation of WNG/PP Separator

As shown in **Figure S13**, commercial PP separator exhibits many unevenly distributed pores, which can be conformally and fully covered by WNG layer through a vacuum filtration. A thin WNG coating layer with a thickness of 7.4 μm was tightly adhered on the surface of PP separator (**Figure S14**). The functionalized WNG/PP separators are completely bendable without detachment of WNG powder (**Figure S14c**), indicating the robustness and flexibility of the coating layer on PP separators. The thermogravimetric analysis of WNG, W<sub>2</sub>N<sub>3</sub>, NG and PP and the thermal stability of PP, NG/PP, W<sub>2</sub>N<sub>3</sub>/PP and WNG/PP separators are also tested in air. It can be observed that WNG, W<sub>2</sub>N<sub>3</sub> and NG exhibited remarkable thermostability up to 500 °C, in sharp contrast, PP becomes unstable at 134 °C (**Figure S15**). Therefore, WNG, W<sub>2</sub>N<sub>3</sub> and NG exhibited high thermostability than that of bare PP. The thermal stability characterization of PP, NG/PP, W<sub>2</sub>N<sub>3</sub>/PP and WNG/PP separators further confirmed this result as **Figure S16**. The thermostability of the WNG/PP separator was evaluated by increasing temperatures from 30 °C to 150 °C in atmosphere. At 150 °C, the PP, NG/PP and W<sub>2</sub>N<sub>3</sub>/PP separators seriously wrinkled in contrast to the almost intact morphology of WNG/PP. It illustrates the superior thermostability for WNG/PP, which is important for the safety of LMBs working under high temperatures. The atomic force microscope (AFM)

Young's modulus mappings demonstrated that the WNG/PP separator has a higher Young's modulus than that of pristine PP separators (**Figure S17**), suggesting that WNG molecular coating has improved mechanical strength, which can reinforce to suppress Li dendrite growth.

The electrolyte wettability was investigated by adding a droplet of 1 M LiTFSI DOL/DME electrolyte onto various separator (**Figure S18**). It is observed that the electrolyte droplet on pristine PP separator retains a hemispherical droplet (**Figure S18a**), in sharp contrast, the electrolyte droplet on WNG/PP separator was immediately absorbed and spread uniformly in all directions (**Figure S18b**). In addition, the contact angle was also tested to further demonstrate the electrolyte wettability of different separator (**Figure S19**). It shows that the contact angle of electrolyte on WNG/PP is around 20°, which is less than half of the 44° for PP separator. Above results indicated that WNG/PP separator has much better electrolyte wettability property in comparison to pristine PP, resulting in comparatively faster electrolyte transport. Furthermore, the electrolyte uptake of the functionalized separator is also determined to be larger than bare PP, leading to the favorable diffusion of Li ions in the liquid electrolyte (**Figure S20**). The improved electrolyte uptake can be ascribed to the pores structure of the WNG layer and the strong interaction between WNG and electrolyte.

The Li-ionic conductivity determines the Li ion migration rate through the separators, which is a key parameter for high-power and dendrite-free LMBs. Electrochemical impedance spectrum (EIS) measurements were performed to test the ionic conductivity of PP, NG/PP, W<sub>2</sub>N<sub>3</sub>/PP and WNG/PP separators (**Figure S21a**). The relevant bulk resistances were obtained from Nyquist curves as presented in **Figure S21b**. The ion conductivities of PP, NG/PP, W<sub>2</sub>N<sub>3</sub>/PP and WNG/PP separators were calculated to be 0.384, 0.661, 0.572, and 1.141 mS cm<sup>-1</sup>, respectively (**Figure**

**S21c**). It clearly demonstrates that functionalized separators, especially WNG/PP separator, displayed discernible enhancement in ionic conductivity compared to bare PP. The higher ionic conductivity of the WNG/PP separator was primarily attributed to the relatively high porosity, abundant ion channels and favorable electrolyte affinity. The Li-ion transference number ( $t_{\text{Li}^+}$ ) is another key indicator to evaluate the performance of separators. Tests were performed to evaluate  $t_{\text{Li}^+}$  of PP and WNG/PP separator (**Figure S22**). The  $t_{\text{Li}^+}$  of the PP and WNG/PP separator was 0.4 and 0.5, respectively (**Table S1**). The higher value in the WNG/PP separator reflects the improvements in Li-ion migration. These results indicate that the WNG coating plays a significant role in improving the transference number and conductivity of Li ions, resulting in significantly enhanced surface lithiophilicity and organophilicity, as well as thermal and chemical stability. All these properties allow us to expect faster Li-ion migration, dendrite-free Li plating behavior, and thus improved safety and the electrochemical performance of LMBs.

#### **2.4 Simulations of Li-ion distribution**

The Li ionic transport and distribution through bare PP and WNG/PP separator is modelled to unveil the uniformed Li deposition. The ion distributions through the bare PP and WNG/PP separator, in which Li ions passing through the separator in the direction of y-axis, are presented in **Figure 3** (see details in **Table S2**). Owing to the negligible Li ion conductivity of the bare PP separator, Li ions are mainly concentrated in the adjacent pores<sup>[45]</sup>. Electrolytes built up in the pores are the only way for the migration of Li ions. As a result, an uneven distribution of Li ion flux will pass through the PP separator during the deposition process (**Figure 3a, c**). It is likely that the fluctuations in ion distribution potentially caused by the failure of partial electrode materials or changes of the local electric field, are difficult to completely avoid in commercial batteries<sup>[23]</sup>.

These issues are unavoidable for bare PP separator, leading to inhomogeneous Li deposition. Conversely, a separator functionalized by WNG layer will have stronger interactions with Li atom as demonstrated before, resulting in a stable and dense Li deposition. Consequently, WNG coated PP separator can regulate and redistribute Li ions through the abundant pores/channels and stronger interactions with Li atom present, leading to a uniform Li distribution and deposition (**Figure 3b, c**). The comparison of the Li ion concentrations in bare PP and WNG/PP separator surface are exhibited in **Figure 3c** and **Table S3**. The standard deviation of the Li ion concentration on the bare PP separator is 11.3 times higher than the WNG/PP separator (**Table S3**). This indicates a large ion concentration fluctuation on the PP separator which will cause an uneven distribution of Li ion. In the WNG/PP separator, the migration of Li ions along the y-direction is accompanied by appreciable transverse diffusion present resulting in a uniform and smooth Li deposition for dendrite-free Li metal batteries.

The mechanism proposed can be illustrated by the schematics as shown in **Figure 3d-e**. The PP separator with irregular pores/channels that will cause an inhomogeneous ionic flux when the Li ion passes through resulting in uneven electric fields. The presence of these will in turn facilitate the growth of the Li dendrites that can penetrate across the separator causing internal short circuiting of the cell (**Figure 3d**). In contrast, when the PP separator is functionalized by WNG layer, the Li ion flux and concentration across the separator were regulated and redistributed. This will be formed homogeneous Li ion flux resulting in uniform and smooth Li deposition (**Figure 3e**), further reducing side reactions and delaying the onset of dendrite nucleation <sup>[46, 47]</sup>.

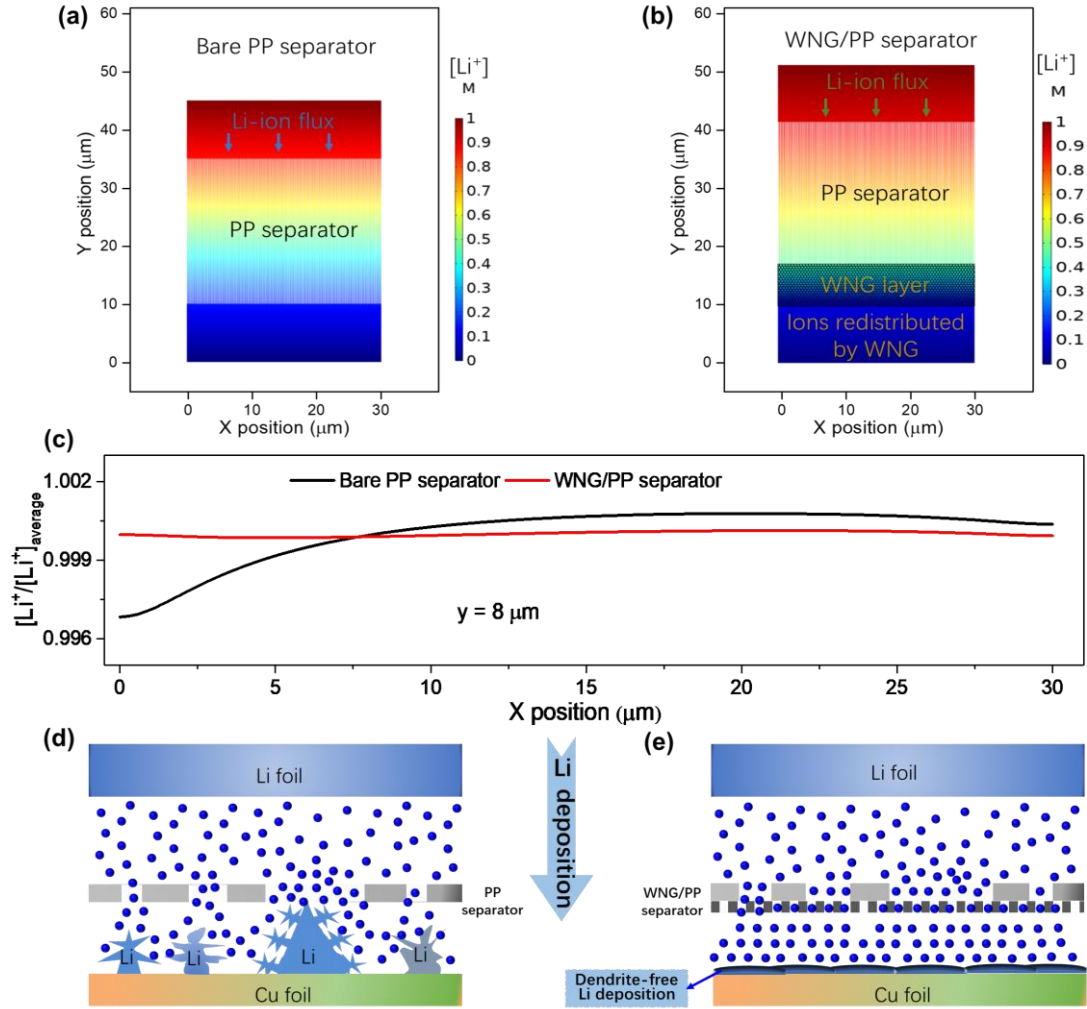


**Figure 3.** Simulations of ionic transport behaviors and dendrite growth in a pristine PP separator and the composite separator with the WNG layer as an ion redistributor. Distributions of Li ions through (a) bare PP separator and (b) WNG composite separator. Colors in the graph represent the concentration of Li ions ( $[Li^+]$ ). The relative concentration of Li ions beneath the bare PP and the WNG/PP separator at  $y = 8 \mu m$  in the FEM simulation results (c).  $[Li^+]_{avg}$  is the average concentration at  $y = 8 \mu m$  for each separator. Schematic representation of the Li ion transport in (d) PP separator cell and (e) WNG/PP composite separator cell.

## 2.5 Symmetrical and Asymmetrical Li Metal Cell Analysis

Due to the unique physiochemical advantages described above, the WNG/PP separator is expected promising for adjusting Li deposition and suppressing Li dendrite growth. Symmetric Li//Li cells equipped with bare PP and WNG/PP separators were assembled to demonstrate the merits of functionalized separators. Long-term Li plating/stripping tests were conducted at the

current density of  $0.8 \text{ mA cm}^{-2}$ ,  $2 \text{ mA cm}^{-2}$  and  $5 \text{ mA cm}^{-2}$  with the deposited capacity of  $0.8 \text{ mAh cm}^{-2}$  and  $1 \text{ mAh cm}^{-2}$ , respectively (**Figure S23, 4a, 4e**). The hysteresis voltage of Li//Li symmetric cells with WNG/PP separator at both  $2 \text{ mA cm}^{-2}$  and  $5 \text{ mA cm}^{-2}$  show fluctuations in the first  $\sim 100$  h (**Figure 4a, 4e**), which could be attributed to the activation among the electrolytes, separator and electrodes as well as the formation of stable SEI layer on the surface of Li metal anodes, consistent with previous reports [48, 49]. Then, the hysteresis voltage of the WNG/PP-based cell gradually decreases and remain stable for more than 1700 h at  $2 \text{ mA cm}^{-2}$  and 2000 h at  $5 \text{ mA cm}^{-2}$ . However, the hysteresis voltage of the symmetrical cell using the PP separator is considerably larger than that of the cell using the WNG/PP separator. The cell equipped with the PP separator had an overpotential of 47 mV during the initial cycles, which gradually increased to 100 mV after 200 h (**Figure 4b, upper**), and more drastically to 150 mV after 370 h indicating a progressive polarization phenomenon. The increasing polarization is likely attributed to the formation of Li dendrites (mossy deposits) which have a larger surface area and can cause rapid consumption of the electrolyte [50]. In contrast, the Li//Li cell with a WNG/PP separator delivered an extremely high cycling stability with a low hysteresis voltage of 15.4 mV over 1700 h (**Figure 4a, b**). This indicates the negligible polarization arising from efficient dendrite inhibition for the Li//Li cell using functionalized separator, which can be assigned to homogeneous Li plating/stripping that contributing to the formation of a uniform and stable SEI [51-53]. The stable polarization during cycling also demonstrates the reversibility of the homogeneous Li plating/stripping process using the WNG/PP separator.

**Figure 4c-d** displays the SEM images of the Li metal anodes using the PP and WNG/PP separators after 100 cycles at  $2 \text{ mA cm}^{-2}$  with capacity of  $1 \text{ mAh cm}^{-2}$ , respectively. Fresh Li foil

was also characterized as a reference, which presented a smooth and dense morphology with minor fish-scale surface features stemming from the polishing process (**Figure S24**). The surface of the cycled Li foil with the PP separator (**Figure 4c**) exhibits significant wire-shaped Li dendrites and loosely stacked mossy Li with a highly porous structure. The surface of the cycled Li anode with a WNG/PP separator (**Figure 4d**) demonstrates a dense and compact Li deposition. The anode surface has smooth edges and does not show any evidence of Li dendrite formation, highlighting the advantages of the WNG/PP separator.

A stability test of the symmetrical cell was conducted at a higher current density ( $5 \text{ mA cm}^{-2}$ ) with a capacity of  $1 \text{ mAh cm}^{-2}$  (**Figure 4e**). The cell equipped with the WNG/PP separator presented excellent long-term stability over 2000 h with smooth and stable cycling plateaus. While the cell equipped with the PP separator demonstrated a continuous increase in polarization and uneven profiles during cycling (**Figure S25**). The WNG/PP separator cell cycled more than 2000 h without any significant increase in the polarization and hysteresis voltage ( $49.6 \text{ mV}$ ). However, the PP separator cell continuously increased the polarization and overpotential from the start of cycling with the overpotential reaching up to  $560 \text{ mV}$  after only 360 h. The cycling stability of the cells at different current densities illustrates potential application of the proposed method under different conditions. EIS spectra of Li//Li symmetrical cells using PP and WNG/PP separators presented in **Figure S26**. The interfacial resistance of the cell using PP and WNG/PP separators was 117 and  $44.5 \text{ }\Omega$ , respectively. The small interfacial resistance of WNG/PP is indicative of the fast ion transfer at the interface, which can be ascribed to the enhanced Li ion mobility due to the favorable electrolyte wettability of the WNG/PP and improved Li transfer number <sup>[54]</sup>.

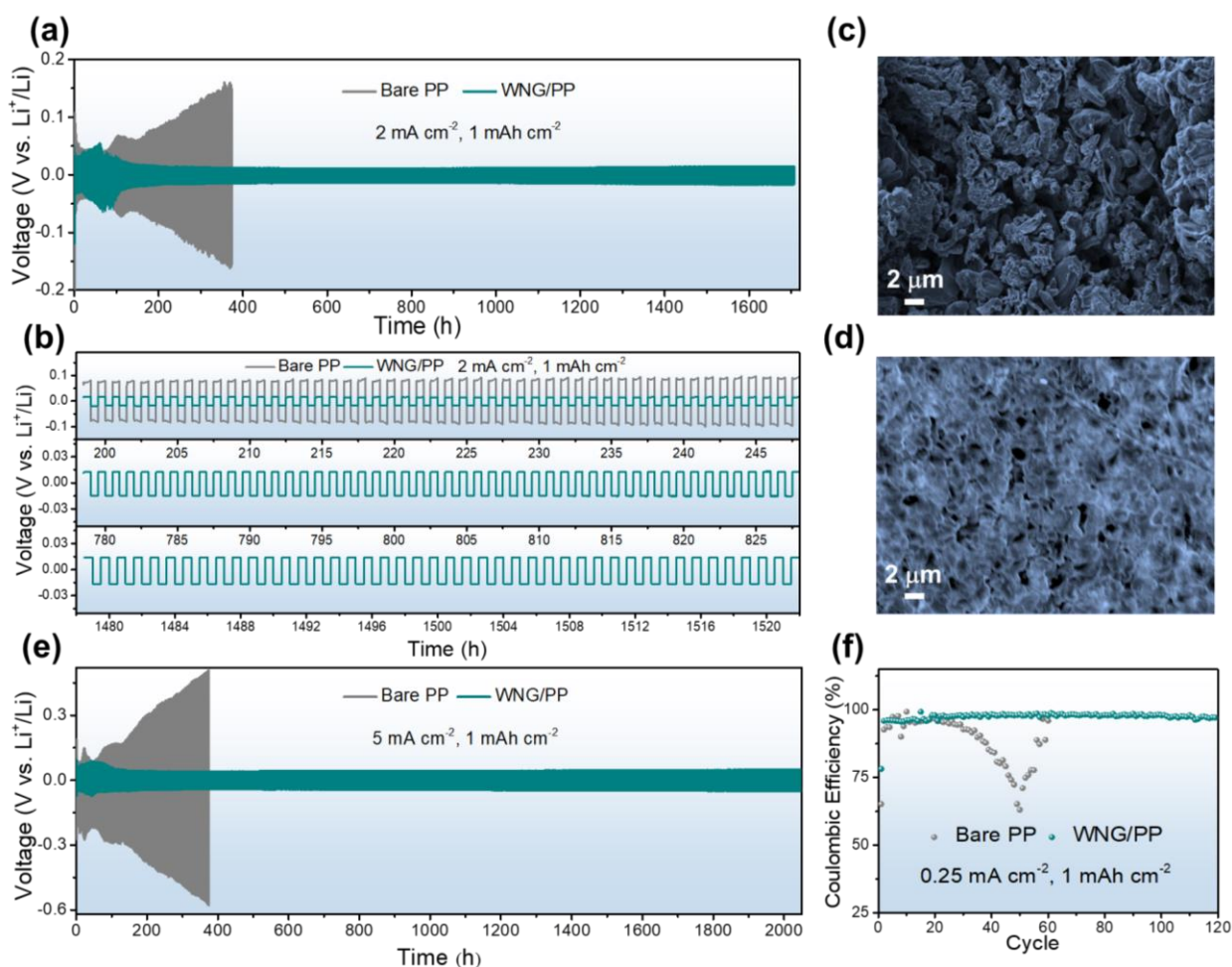


**Figure 4.** Electrochemical performance of bare PP and WNG/PP separators for Li metal anodes. (a) Galvanostatic Li plating/stripping of symmetrical cells equipped with WNG/PP and bare PP separators at  $2.0 \text{ mA} \cdot \text{cm}^{-2}$  with  $1.0 \text{ mAh} \cdot \text{cm}^{-2}$ , (b) Zoomed voltage profile at different time intervals. SEM images of Li foils (c) after cycling with PP separator and (d) WNG/PP separator. (e) galvanostatic Li plating/stripping of symmetrical cells equipped with WNG/PP and bare PP separators at  $5 \text{ mA} \cdot \text{cm}^{-2}$  with  $1.0 \text{ mAh} \cdot \text{cm}^{-2}$ , (f) Coulombic efficiency of Li//Cu cells equipped with WNG/PP and bare PP separators with a cycling capacity of  $1 \text{ mAh} \cdot \text{cm}^{-2}$  at  $0.25 \text{ mA} \cdot \text{cm}^{-2}$ .

The Coulombic Efficiencies of Li//Cu cells equipped with PP and WNG/PP separators were tested at different current densities with a deposited areal capacity of  $1 \text{ mAh} \cdot \text{cm}^{-2}$ . Under these conditions the deposited Li is completely stripped from the Cu foils with a cut-off voltage of 0.5 V. As displayed in **Figure 4f**, the Li//Cu cell with WNG/PP separator displays a high and steady Coulombic efficiency of 97.2% over 120 cycles at a current density of  $0.25 \text{ mA} \cdot \text{cm}^{-2}$ . While Coulombic efficiency of PP separator retains only a 63.2% after 50 cycles. At current densities of

0.5 mA cm<sup>-2</sup> and 1 mA cm<sup>-2</sup>, the cell with the WNG/PP separator also presents a high and steady Coulombic efficiency of 95.3% (over 85 cycles) and 95.2% (over 65 cycles), respectively. In comparison, cells with the PP separator exhibit significantly worse electrochemical cycling stability with severe fluctuations in Coulombic efficiencies exhibited during Li plating/stripping processes (**Figure 4f, S27**). These fluctuations may be caused by successive destruction/reconstruction of the SEI, which will lead to a deterioration and consumption of Li and electrolyte <sup>[55]</sup>.

Ex-situ SEM characterization was conducted to investigate the morphology evolution of deposited Li on Cu foil using PP (WNG/PP) separator at a current density of 0.5 mA cm<sup>-2</sup> with different deposited Li capacities. This was conducted to verify the effects of the WNG/PP separator on suppression of Li dendrites during plating/stripping cycling. SEM image of fresh Cu foil demonstrated that the substrate had a smooth surface and was free of residual contamination (**Figure S28**). SEM images of deposited Li metal on Cu foil for cells with PP separator is presented in **Figure 5a-d**. Micrometer-sized Li particles were inhomogeneous in size and deposited on the surface of Cu foil during the initial nucleation period (**Figure 5a**). When charge gathers at these positions in the electric field, these Li particles will act as nucleation sites in the following Li deposition process. As Li is continuously deposited, dendritic filaments will sprout out from the particles and developed into sharper, randomly oriented dendrites (**Figure 5b-d**). The Li plating behavior indicates the significant formation and growth of Li dendrites in the cell with the PP separator. In the subsequent stripping process, the dendritic filaments become slender and sectional until voltage reached up to 0.5 V (**Figure 5j**). After repeating this cycling 10 times, there was a larger quantity of dendrite present and a significant quantity of “dead Li” on the Cu foil surface (**Figure 5k, l**).

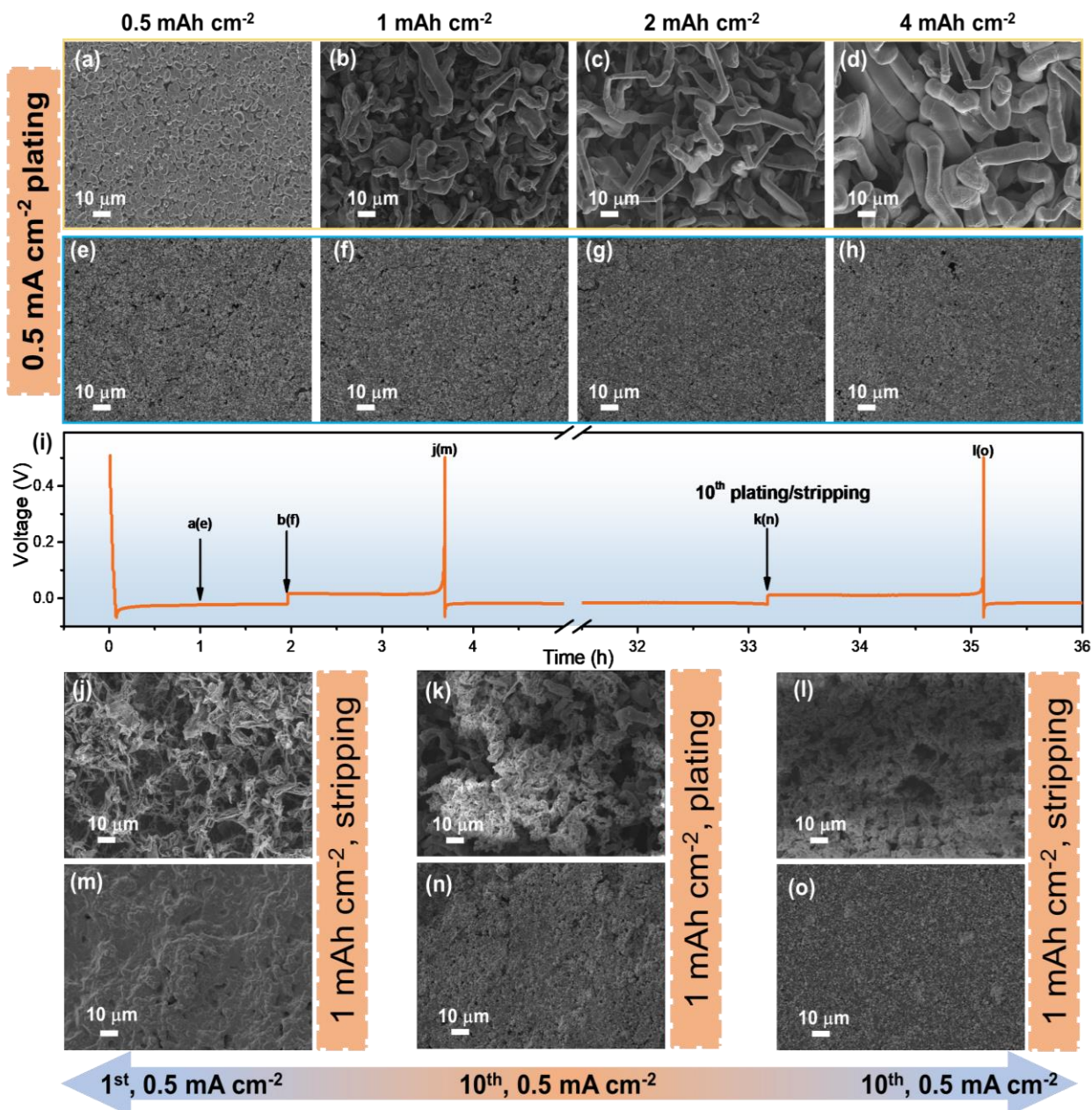


**Figure 5.** Morphology evolution of Li//Cu cells with bare PP and WNG/PP separator during plating/stripping. After plating (a)  $0.5 \text{ mAh cm}^{-2}$ , (b)  $1 \text{ mAh cm}^{-2}$ , (c)  $2 \text{ mAh cm}^{-2}$ , (d)  $4 \text{ mAh cm}^{-2}$  at a current rate of  $0.5 \text{ mA cm}^{-2}$  with bare PP and (e)  $0.5 \text{ mAh cm}^{-2}$ , (f)  $1 \text{ mAh cm}^{-2}$ , (g)  $2 \text{ mAh cm}^{-2}$ , (h)  $4 \text{ mAh cm}^{-2}$  at a current rate of  $0.5 \text{ mA cm}^{-2}$  with WNG/PP separator. (i) The corresponding discharge-charge curve. SEM images of deposited Li on Cu electrode after the first stripping of (j) bare PP and (m) WNG/PP separator. SEM images of deposited Li on Cu electrode after (k, n) the 10th plating and (l, o) the 10th stripping of bare PP and WNG/PP separator, respectively.

In contrast, the shape and size of deposited Li on Cu foil surfaces from the cell with the WNG/PP separator is significantly different from those on PP separator cell. The morphology of

deposited Li at increasing of plating capacities is exhibited in **Figure 5e-h**. When the capacity is  $0.5 \text{ mAh cm}^{-2}$ , a dense and homogeneous distribution of Li particles is present on the Cu foil (**Figure 5e**). When the plating capacity is increased up to  $4 \text{ mAh cm}^{-2}$ , uniform and dense particles can be observed with the same morphology of the initial nucleating stage (**Figure 5f-h**). And the surface keeps flat and dense after the stripping (**Figure 5m**). These results illustrate the inhibition of dendrite growth, providing evidence for the mechanisms of suppression discussed above. After 10 plating cycles at a capacity of  $1.0 \text{ mAh cm}^{-2}$ , the surface of the deposited Li was still smooth and uniform (**Figure 5n**). After stripping and recharging to  $0.5 \text{ V}$ , the surface of the Cu substrate was still dense and smooth, leading to a reversible Li consumption (**Figure 5o**) and resulting in enhanced CE of plating/stripping.

## 2.6 Lithium Metal Full Cells

To further confirm the applicability of the WNG/PP separator in LMBs, the full cells were assembled using bare Li foil anode with commercial  $\text{LiFePO}_4$  cathodes and PP or WNG/PP separators, as presented in **Figure 6, S29**. **Figure S29a** displays the 10<sup>th</sup> charge/discharge profiles of the Li//LFP full cells with PP, NG/PP,  $\text{W}_2\text{N}_3/\text{PP}$  and WNG/PP separators at a current rate of  $0.5\text{C}$ . The discharge capacities are 151, 141, 138 and  $134 \text{ mAh g}^{-1}$ , respectively, indicating that the functionalized separator can improve the utilization of Li. The rate performances of the cells with bare PP and WNG/PP separator were investigated at rates from  $0.2$  to  $3\text{C}$ , as presented in **Figure 6a-b**. The bell-shaped charge/discharge curves for both full cells were observed. Compared to the PP separator, the full cells with WNG/PP separator allowed for small polarization at all rates (**Figure S29b**), which can be ascribed to enhanced kinetics from suppressing dendrite formation and continuous electrolyte consumption<sup>[23]</sup>. The cell with the WNG/PP separator delivered higher

capacities at rates from 0.2 to 3C compared to the cell with bare PP separator (**Figure S29c**). This result illustrates the high utilization of cathodic active material of the cell equipped with WNG/PP separator. **Figure 6c-e** displays the long-term cycling stability of cells with bare PP and WNG/PP separator at rates from 1 to 3C. The initial specific capacities of cells with the WNG/PP separators are 135.9, 107.6 and 92.4 mAh g<sup>-1</sup> at 1C, 2C and 3C, which maintains an excellent cycling performance of 82.1%, 72.3% and 63.5% capacity retention with average CEs of 98.8%, 98.2% and 98.1% until after 300 cycles, respectively. These values are superior or comparable to previously reported data pertaining to full cells with modified separators (**Table S4**). However, for full cell with PP separator, the capacity retention drops dramatically below 40% in less than 60 cycles, especially at high rate of 3C (**Figure 6e**). As to the cell with a WNG/PP separator, some portion of the applied current participates in the lithiation-delithiation of graphene nanosheets, which relatively reduces the local current density being applied to the cathode electrode <sup>[54]</sup>. The reduced current density improves the entire electrochemical stabilities and performances of the full cell. Moreover, the formed graphene layer offers an additional conductive pathway to the counter electrode, facilitating the enhanced electrochemical reactions of the cathode electrode, and thus resulting in improved utilization of active material, which enhanced the specific capacity. The drastic reduction in capacity is due to the formation of large amounts of dendritic structures and dead Li (high surface area), which consumes a lot of electrolyte with the side reaction. While in the WNG/PP separator cells, the capacity decreased gradually, attributed to the formation of dendrite-free structures and slow consumption of the electrolyte. To verify the suppression of dendrites, top-view SEM images of Li metal anodes of the full cells after 300 cycles were conducted (**Figure 6f-i**). The cycled Li anode from the PP separator cell exhibited sharp dendrites with the large and

porous holes, as well complete disappearance of the original Li metal shape (**Figure 6f, g**). This result indicated that Li dendrite was generated during the whole cycling leading to repeated reconstruction of the SEI layer. In contrast, owing to the WNG interlayer redistributed and regulated the concentration and flux of Li ions by stronger adsorption interactions, the surface of the Li anode disassembled from the WNG/PP separator cell shows the smooth and compact deposited Li without any traces of dendrites (**Figure 6h, i**).

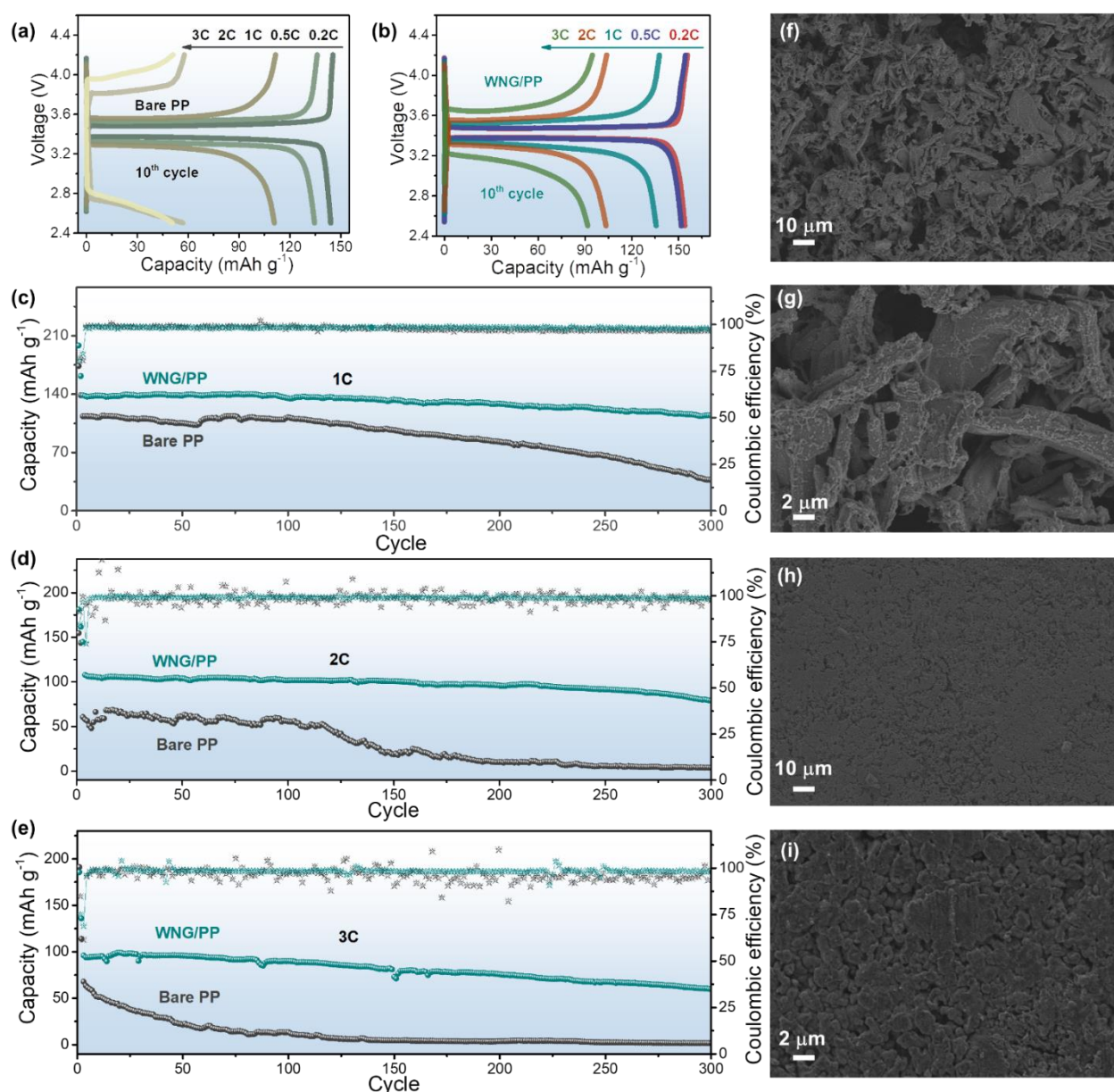


**Figure 6.** Full cells with Li anode and LiFePO<sub>4</sub> (LFP) cathode. Typical discharge-charge profiles of the Li//LFP cells equipped with (a) bare PP and (b) WNG/PP separators at current rate from 0.2C

to 3C. Long-term cycling stability and Coulombic efficiency of Li//LFP full cells with pristine PP, and WNG/PP separator at (c) 1C, (d) 2C, and (e) 3C, the first cycle is activated at 0.1C. SEM images of Li foil disassembled full cells with (f, g) PP separator and (h, i) WNG/PP separator after 300 cycles at 1C.

### 3. Conclusions

In summary, a promotable approach to inhibit the formation of Li dendrites was demonstrated in this work by coating a mechanically and chemically stable WNG interlayer on the PP separator was demonstrated. The WNG interlayer redistributes and regulates the concentration and flux of Li ions by stronger adsorption interaction during charging/discharging process, resulting in dendrite-free Li anode. The WNG/PP separator can also mechanically inhibit the growth of Li dendrite, evident by the high modulus. Thanks to these ameliorating features of the WNG/PP separator, superior long-term stability of Li plating/stripping in symmetrical Li//Li cell over 2100 h was achieved at a high current density of  $5 \text{ mA cm}^{-2}$  with a small polarization voltage of 49.6 mV. Remarkably, the Li//LFP full cell based on the WNG/PP separator renders excellent electrochemical performance of high specific capacity of  $135.9 \text{ mAh g}^{-1}$  at 1C and more than 300 stable cycles with a capacity retention of 82.1% and a CE of 98.8%, demonstrating the feasibility of using polar WNG as ion redistributors and regulators in LMBs. The theoretical and experimental results illustrate that this simple and effective approach can also be expanded to other alkaline metal battery facing the similar challenges.

### EXPERIMENTAL PROCEDURES

The data that support the findings of this work are available in the main text and the **supplemental information**, including: materials and methods, experimental procedures, computational and simulation methods, **Figures S1–S31**, the predicted configurations, Schematic illustration of Li dendritic growth behaviors,  $\text{N}_2$  adsorption/desorption isotherms, SEM and XRD of precursor, XPS

full spectrum, Cross-section of the WNG/PP separator, Optical photographs of the WNG/PP separator under various folds, thermal stability characterization, AFM Young's modulus mappings, Optical photographs of Wettability, contact angle characterization, Electrolyte uptake test, Li-ion conductivity test, Zoomed voltage profile, EIS of symmetrical cells, Coulombic efficiency and Typical discharge-charge profiles of the Li//LFP full cells are available from supporting information.

### **Conflict of Interest**

The authors declare no conflict of interest.

### **Acknowledgements**

The work described in this paper was supported by grants from the National Natural Science Foundation of China (Project Nos. 21773024, 52102310), Sichuan Science and Technology program (Grant Nos. 2020YJ0324, 2020YJ0262), Reformation and Development Funds for Local Region Universities from China Government in 2020 (Grant No. ZCKJ 2020-11), and the China Postdoctoral Science Foundation (Grant No. 2019M663469), and Academic support program for doctoral students of University of Electronic Science and Technology of China (Grant No. Y03019023901001). The work described in this paper is partially supported by grants from the Research Committee at the Hong Kong Polytechnic University under Project Codes of BE3M, BBXK and PB1M. The authors would like to express their gratitude to EditSprings (<https://www.editsprings.cn/>) for the expert linguistic services provided. The authors would like to thank Ting Du from Shiyanjia Lab ([www.shiyanjia.com](http://www.shiyanjia.com)) for the infrared thermal imaging, TG, and XPS test.

## References

- [1] J. Tan, X. Ao, A. Dai, Y. Yuan, H. Zhuo, H. Lu, L. Zhuang, Y. Ke, C. Su, X. Peng, B. Tian, J. Lu, Polycation ionic liquid tailored PEO-based solid polymer electrolytes for high temperature lithium metal batteries, *Energy Storage Materials* 33 (2020) 173.
- [2] X. Miao, H. Wang, R. Sun, C. Wang, Z. Zhang, Z. Li, L. Yin, Interface engineering of inorganic solid-state electrolytes for high-performance lithium metal batteries, *Energ. Environ. Sci.* 13 (2020) 3780.
- [3] B. Liu, J. Zhang, W. Xu, Advancing Lithium Metal Batteries, *Joule* 2 (2018) 833.
- [4] Z. Xu, S. J. Kim, D. Chang, K. Park, K. S. Dae, K. P. Dao, J. M. Yuk, K. Kang, Visualization of regulated nucleation and growth of lithium sulfides for high energy lithium sulfur batteries, *Energ. Environ. Sci.* 12 (2019) 3144.
- [5] Q. Wang, B. Liu, Y. Shen, J. Wu, Z. Zhao, C. Zhong, W. Hu, Confronting the challenges in lithium anodes for lithium metal batteries, *Adv Sci* (2021) 2101111.
- [6] Z. Xu, J. Kim, K. Kang, Carbon nanomaterials for advanced lithium sulfur batteries, *Nano Today* 19 (2018) 84.
- [7] B. Yu, A. Huang, D. Chen, K. Srinivas, X. Zhang, X. Wang, B. Wang, F. Ma, C. Liu, W. Zhang, J. He, Z. Wang, Y. Chen, In Situ Construction of Mo<sub>2</sub>C Quantum Dots-Decorated CNT Networks as a Multifunctional Electrocatalyst for Advanced Lithium–Sulfur Batteries, *Small* 17 (2021) 2100460.
- [8] Z. Li, Q. He, C. Zhou, Y. Li, Z. Liu, X. Hong, X. Xu, Y. Zhao, L. Mai, Rationally design lithiophilic surfaces toward high-energy Lithium metal battery, *Energy Storage Materials* 37 (2021) 40.
- [9] P. Albertus, S. Babinec, S. Litzelman, A. Newman, Status and challenges in enabling the lithium metal electrode for high-energy and low-cost rechargeable batteries, *Nat. Energy* 3 (2018) 16.
- [10] S. Wei, S. Choudhury, Z. Tu, K. Zhang, L. A. Archer, Electrochemical interphases for high-energy storage using reactive metal anodes, *Accounts Chem Res* 51 (2018) 80.
- [11] D. Cao, Y. Zhao, X. Sun, A. Natan, Y. Wang, P. Xiang, W. Wang, H. Zhu, Processing strategies to improve cell-level energy density of metal sulfide electrolyte-based all-solid-state lithium metal batteries and beyond, *ACS Energy Lett* 5 (2020) 3468.

- [12] Y. Zhu, J. Cao, H. Chen, Q. Yu, B. Li, High electrochemical stability of a 3D cross-linked network PEO@nano-SiO<sub>2</sub> composite polymer electrolyte for lithium metal batteries, *J Mater Chem A* 7 (2019) 6832.
- [13] Q. Zhao, Z. Tu, S. Wei, K. Zhang, S. Choudhury, X. Liu, L. A. Archer, Building organic/inorganic hybrid interphases for fast interfacial transport in rechargeable metal batteries, *Angew. Chemie Interna. Edition* 57 (2018) 992.
- [14] Y. Lu, Z. Tu, L. A. Archer, Stable lithium electrodeposition in liquid and nanoporous solid electrolytes, *Nat. Mater.* 13 (2014) 961.
- [15] S. Li, Z. Luo, H. Tu, H. Zhang, W. Deng, G. Zou, H. Hou, X. Ji, N, S-codoped carbon dots as deposition regulating electrolyte additive for stable lithium metal anode, *Energy Storage Materials* 42 (2021) 679.
- [16] C. Lin, Y. Qi, K. Gregorczyk, S. B. Lee, G. W. Rubloff, Nanoscale protection layers to mitigate degradation in high-energy electrochemical energy storage systems, *Accounts Chem Res* 51 (2018) 97.
- [17] A. Hu, W. Chen, X. Du, Y. Hu, T. Lei, H. Wang, L. Xue, Y. Li, H. Sun, Y. Yan, J. Long, C. Shu, J. Zhu, B. Li, X. Wang, J. Xiong, An artificial hybrid interphase for an ultrahigh-rate and practical lithium metal anode, *Energ. Environ. Sci.* 14 (2021) 4115.
- [18] O. Sheng, J. Zheng, Z. Ju, C. Jin, Y. Wang, M. Chen, J. Nai, T. Liu, W. Zhang, Y. Liu, X. Tao, In-situ construction of a LiF-enriched interface for stable all-solid-state batteries and its origin revealed by Cryo-TEM, *Adv. Mater.* 32 (2020) 2000223.
- [19] Q. Li, S. Zhu, Y. Lu, 3D porous Cu current collector/Li-metal composite anode for stable lithium-metal batteries, *Adv. Funct. Mater.* 27 (2017) 1606422.
- [20] R. Zhang, X. Cheng, C. Zhao, H. Peng, J. Shi, J. Huang, J. Wang, F. Wei, Q. Zhang, Conductive nanostructured scaffolds render low local current density to inhibit lithium dendrite growth, *Adv Mater* 28 (2016) 2155.
- [21] Z. Luo, S. Li, L. Yang, Y. Tian, L. Xu, G. Zou, H. Hou, W. Wei, L. Chen, X. Ji, Interfacially redistributed charge for robust lithium metal anode, *Nano Energy* 87 (2021) 106212.
- [22] Y. Liu, Q. Liu, L. Xin, Y. Liu, F. Yang, E. A. Stach, J. Xie, Making Li-metal electrodes rechargeable by controlling the dendrite growth direction, *Nat. Energy* 2 (2017).
- [23] C. Z. Zhao, P. Y. Chen, R. Zhang, X. Chen, B. Q. Li, X. Q. Zhang, X. B. Cheng, Q. Zhang,

- An ion redistributor for dendrite-free lithium metal anodes, *Sci. Adv.* 4 (2018) t3446.
- [24] M. Ryou, D. J. Lee, J. Lee, Y. M. Lee, J. Park, J. W. Choi, Excellent cycle life of lithium-metal anodes in lithium-ion batteries with mussel-inspired polydopamine-coated separators, *Adv. Energy Mater.* 2 (2012) 645.
- [25] J. Jeong, J. Lee, J. Kim, J. Chun, D. Kang, S. M. Han, C. Jo, J. Lee, A biopolymer-based functional separator for stable Li metal batteries with an additive-free commercial electrolyte, *J Mater Chem A* 9 (2021) 7774.
- [26] W. Luo, L. Zhou, K. Fu, Z. Yang, J. Wan, M. Manno, Y. Yao, H. Zhu, B. Yang, L. Hu, A Thermally conductive separator for stable li metal anodes, *Nano Lett* 15 (2015) 6149.
- [27] W. Na, A. S. Lee, J. H. Lee, S. S. Hwang, E. Kim, S. M. Hong, C. M. Koo, Lithium dendrite suppression with uv-curable polysilsesquioxane separator binders, *ACS Appl. Mater. Inter.* 8 (2016) 12852.
- [28] X. Zhu, X. Jiang, X. Ai, H. Yang, Y. Cao, A highly thermostable ceramic-grafted microporous polyethylene separator for safer lithium-ion batteries, *ACS Appl. Mater. Inter.* 7 (2015) 24119.
- [29] J. Xie, L. Liao, Y. Gong, Y. Li, F. Shi, A. Pei, J. Sun, R. Zhang, B. Kong, R. Subbaraman, J. Christensen, Y. Cui, Stitching h-BN by atomic layer deposition of LiF as a stable interface for lithium metal anode, *Sci. Adv.* 3 (2017) o3170.
- [30] C. Li, S. Liu, C. Shi, G. Liang, Z. Lu, R. Fu, D. Wu, Two-dimensional molecular brush-functionalized porous bilayer composite separators toward ultrastable high-current density lithium metal anodes, *Nat. Commun.* 10 (2019).
- [31] Y. Guo, H. Li, T. Zhai, Reviving lithium-metal anodes for next-generation high-energy batteries, *Adv. Mater.* 29 (2017) 1700007.
- [32] D. Choi, P. N. Kumta, Synthesis, structure, and electrochemical characterization of nanocrystalline tantalum and tungsten nitrides, *J. Am. Ceram. Soc.* 90 (2007) 3113.
- [33] A. M. A. Q. Memon, Idrees, Transition metal nitride electrodes as future energy storage devices: a review, *Materials Today Communications* (2021) 102363.
- [34] D. H. S. M. Y. Kwak, Characteristics of WN diffusion barrier layer for copper metallization, *phys. Stat. Sol.* 174 (1999) R5.
- [35] Y. Liu, Q. Liu, L. Xin, Y. Liu, F. Yang, E. A. Stach, J. Xie, Making Li-metal electrodes rechargeable by controlling the dendrite growth direction, *Nat. Energy* 2 (2017).

- [36]D. Campi, S. Kumari, N. Marzari, Prediction of phonon-mediated superconductivity with high critical temperature in the two-dimensional topological semimetal  $W_2N_3$ , *Nano Lett* 21 (2021) 3435.
- [37]Y. Wang, E. Zhao, J. Zhao, L. Fu, C. Ying, L. Lin, Prediction of novel ground state and high pressure phases for  $W_2N_3$ : First principles, *Computational Materials Sci.* 156 (2019) 215-223.
- [38]T.S. Wang, X. Liu, X. Zhao, P. He, C. W. Nan, L. Z. Fan, Regulating uniform Li plating/stripping via dual-conductive metal-organic frameworks for high-rate lithium metal batteries, *Adv. Funct. Mater.* 30 (2020) 2000786.
- [39]S. Wang, X. Yu, Z. Lin, R. Zhang, D. He, J. Qin, J. Zhu, J. Han, L. Wang, H. Mao, J. Zhang, Y. Zhao, Synthesis, crystal structure, and elastic properties of novel tungsten nitrides, *Chem. Mater.* 24 (2012) 3023.
- [40]H. Jin, L. Li, X. Liu, C. Tang, W. Xu, S. Chen, L. Song, Y. Zheng, S. Z. Qiao, Nitrogen vacancies on 2D layered  $W_2N_3$ : a stable and efficient active site for nitrogen reduction reaction, *Adv. Mater.* 31 (2019) 1902709.
- [41]H. Yu, X. Yang, X. Xiao, M. Chen, Q. Zhang, L. Huang, J. Wu, T. Li, S. Chen, L. Song, L. Gu, B. Y. Xia, G. Feng, J. Li, J. Zhou, Atmospheric-Pressure Synthesis of 2D Nitrogen-Rich Tungsten Nitride, *Adv Mater* 30 (2018) 1805655.
- [42]S. Gong, J. Fan, V. Cecen, C. Huang, Y. Min, Q. Xu, H. Li, Noble-metal and cocatalyst free  $W_2N/C/TiO$  photocatalysts for efficient photocatalytic overall water splitting in visible and near-infrared light regions, *Chem Eng J* 405 (2021) 126913.
- [43]H. Yan, C. Tian, L. Sun, B. Wang, L. Wang, J. Yin, A. Wu, H. Fu, Small-sized and high-dispersed WN from  $[SiO_4(W_3O_9)_4]^{4-}$  clusters loading on GO-derived graphene as promising carriers for methanol electro-oxidation, *Energy Environ. Sci.* 7 (2014) 1939.
- [44]B. Yu, D. Chen, Z. Wang, F. Qi, X. Zhang, X. Wang, Y. Hu, B. Wang, W. Zhang, Y. Chen, J. He, W. He,  $Mo_2C$  quantum dots@graphene functionalized separator toward high-current-density lithium metal anodes for ultrastable Li-S batteries, *Chem. Eng. J.* 399 (2020) 125837.
- [45]W. G. Zeier, Structural limitations for optimizing garnet-type solid electrolytes: a perspective, *Dalton Trans.* 43 (2014) 16133.
- [46]Y. Tada, M. Sato, N. Takeno, Y. Nakacho, K. Shigehara, Attempts at lithium single-ionic conduction by anchoring sulfonate anions as terminating groups of oligo(oxyethylene) side chains in comb-type polyphosphazenes, *Chem Mater* 6 (1994) 27.

- [47] S. Rajendran, Z. Tang, A. George, A. Cannon, C. Neumann, A. Sawas, E. Ryan, A. Turchanin, L. M. R. Arava, Inhibition of lithium dendrite formation in lithium metal batteries via regulated cation transport through ultrathin sub-nanometer porous carbon nanomembranes, *Adv. Energy Mater.* (2021) 2100666.
- [48] Z. Li, M. Peng, X. Zhou, K. Shin, S. Tunmee, X. Zhang, C. Xie, H. Saitoh, Y. Zheng, Z. Zhou, Y. Tang, In Situ Chemical Lithiation Transforms Diamond-Like Carbon into an Ultrastrong Ion Conductor for Dendrite-Free Lithium-Metal Anodes, *Adv Mater* 33 (2021) 2100793.
- [49] T. Xu, P. Gao, P. Li, K. Xia, N. Han, J. Deng, Y. Li, J. Lu, Fast-charging and ultrahigh-capacity lithium metal anode enabled by surface alloying, *Adv. Energy Mater.* 10 (2020) 1902343.
- [50] X. Cheng, H. Peng, J. Huang, R. Zhang, C. Zhao, Q. Zhang, Dual-phase lithium metal anode containing a polysulfide-induced solid electrolyte interphase and nanostructured graphene framework for lithium-sulfur batteries, *ACS Nano* 9 (2015) 6373.
- [51] X. Li, Z. Chu, H. Jiang, Y. Dai, W. Zheng, A. Liu, X. Jiang, G. He, Redistributing Li-ion flux and homogenizing Li-metal growth by N-doped hierarchically porous membranes for dendrite-free Lithium metal batteries, *Energy Storage Materials* 37 (2021) 233.
- [52] Y. Yang, J. Zhang, Layered nanocomposite separators enabling dendrite-free lithium metal anodes at ultrahigh current density and cycling capacity, *Energy Storage Materials* 37 (2021) 135.
- [53] X. Zhang, F. Ma, K. Srinivas, B. Yu, X. Chen, B. Wang, X. Wang, D. Liu, Z. Zhang, J. He, Y. Chen,  $\text{Fe}_3\text{N}@\text{N}$ -doped graphene as a lithiophilic interlayer for highly stable lithium metal batteries, *Energy Storage Materials* 45 (2022) 656.
- [54] P. J. Kim, V. G. Pol, High performance lithium metal batteries enabled by surface tailoring of polypropylene separator with a polydopamine/graphene layer, *Adv Energy Mater* 8 (2018) 1802665.
- [55] X. Zhang, Y. Chen, B. Yu, B. Wang, X. Wang, W. Zhang, D. Yang, J. He, Lithiophilic 3D VN@N-rGO as a multifunctional interlayer for dendrite-free and ultrastable lithium-metal batteries, *ACS Appl Mater Inter* 13 (2021) 20125.